

MS ASHLEY HILMAS (Orcid ID : 0000-0001-7323-1588)

PROFESSOR KATHLEEN SEVENER (Orcid ID : 0000-0002-0753-721X)

DR JOHN W HALLORAN (Orcid ID : 0000-0002-1913-6886)

Article type : Article

Mail id: amhilmas@umich.edu

Damage evolution in SiC/SiC unidirectional composites by X-ray tomography

A. M. Hilmas, K. M. Sevener, J.W. Halloran

Department of Materials Science and Engineering

University of Michigan, Ann Arbor MI

ABSTRACT

Melt infiltrated SiC/SiC CMC unidirectional composite specimens were imaged under load using x-ray micro tomography techniques in order to visualize the evolution of damage accumulation and to quantify damage mechanisms within the composite such as matrix cracking and fiber breaking. The data obtained from these in situ tensile tests were used in comparison with current models and literature results. 3D tomography images were used to measure the location and spacing of matrix cracking that occurred at increasing stress increments during testing within two unidirectional composite specimens. The number of broken fibers and the location of each fiber break gap that occurred within the volume of both specimens was also quantified. The three-dimensional locations of fiber breaks were correlated to the location of each matrix crack within the volume of the specimen and it was found that at the stress scanned directly before failure, most of the fiber breaks occur within 100 microns of a matrix crack.

This is the author manuscript accepted for publication and has undergone full peer review but has not been through the copyediting, typesetting, pagination and proofreading process, which may lead to differences between this version and the [Version of Record](#). Please cite this article as [doi: 10.1111/JACE.17017](https://doi.org/10.1111/JACE.17017)

This article is protected by copyright. All rights reserved

INTRODUCTION

Because of their high temperature capabilities and improved fracture toughness, SiC/SiC ceramic matrix composites (CMCs) are currently being developed and utilized for high-temperature structural applications such as hot section components in gas turbine engines.¹⁻⁴ These composites can sustain a great deal of damage in the form of matrix cracks and fiber fractures, while still maintaining load-carrying ability. Better understanding of damage accumulation such as the number and location of matrix cracks and fiber breaks within the volume of the specimen is needed to increase confidence in life prediction and to provide experimental observations to contrast with mechanical models.⁵⁻¹²

Typically, damage accumulation in CMCs is directly observed using surface microscopy techniques either *in situ* or post fracture.¹³⁻¹⁶ For example, damage mechanisms such as crack opening displacement and matrix crack density have been studied using DIC and manual crack opening displacement measurements by Sevener et. al.¹⁷ They used these measurements to study the *in-situ* progression of matrix cracking in woven SiC/SiC CMCs under tensile load using an SEM and DIC techniques. Other nondestructive methods, such as acoustic emission (AE) and electrical resistance (ER) have been utilized to study types of damage that occur in CMCs under various types of loading and environmental conditions.¹⁸⁻²² The use of x-ray computed microtomography to observe damage in various types of CMCs has proven to be a valuable non-destructive techniques.²³⁻³⁰

Here detailed observations of matrix cracks and fiber breaks are presented from two unidirectional SiC/SiC ceramic matrix composites, using synchrotron x-ray tomography. This work allows for damage accumulation to be observed *in situ* under tensile load using the apparatus developed by Bale et al.²³ Most CMC studies done in relation to micro-CT have been done on minicomposite specimens because smaller sample sizes allow for the specimens to rotate as close to the detector as possible in order to achieve higher resolution images. However, for these experiments, unidirectional laminate specimens were prepared from macroscopic panels of 8-ply $[0^\circ/90^\circ]_s$ MI SiC/SiC HiPerComp™ CMC, manufactured by GE Aviation. The HiPerComp™ composites are made up of Hi-Nicalon Type S fibers with a CVD BN

coating and a dense matrix consisting of SiC and free Si. To obtain the unidirectional composite samples that were imaged, the 8-ply macroscopic specimens were ground and polished until they consisted of only two 0° longitudinal center plies which are contained in the SiC and free silicon melt-infiltrated matrix and a center matrix only rich region. Each fiber tow contained approximately 500 filaments and the fiber volume fraction in each ply was 28% with an average fiber diameter of 15 μm . This correlates well to other studies done showing fiber diameters ranging from 12 – 15 μm .³¹⁻³⁴ The final dimensions of the unidirectional composite specimens were 9 x 3 x 0.4 mm as shown in Figure 1.

EXPERIMENTAL PROCEDURE

In-situ tensile testing during x-ray imaging of a unidirectional SiC/SiC composite was performed on unidirectional SiC/SiC composite specimens at the Advanced Light Source (ALS) at Lawrence Berkeley National Laboratory. The tensile load cell was connected to a portable rotation stage to allow for necessary rotation during imaging and each scan took roughly 10-15 minutes. The apparatus was inserted at the end of tomography beamline 8.3.2. which is often used for tomography imaging and specific details on the test apparatus have been previously documented.^{23,29,30} The load cell has a maximum force of 2kN in the vertical direction with a minimum incremental step of 0.1 μm . During testing, it is crucial to make sure the specimen is aligned accurately within the tensile load cell to avoid undesired reconstruction artifacts in the final images. Checking of the alignment of the specimen was done by visually monitoring the position of the specimen in radiography as the tensile load cell apparatus was rotated 180°.

During specimen scans, the tensile test was paused, and the displacement was held constant at each stress increment in order to record the tomography images. The stress increments at which each specimen was scanned were chosen with the accompaniment of acoustic emissions (AE). Acoustic emission signals were displayed in real time during the tensile testing which allowed for the specimens to be scanned at stress increments where AE sensors picked up a substantial amount of “noise” or AE signals which indicated damage events. The samples were loaded using displacement control and images were taken once either visible damage was observed in the live x-ray imaging or AE signals were detected. This also allowed

for both specimens to be scanned directly after the first through thickness matrix crack had formed. Work was done by Maillet et al on detailing the observations and the comparison of damage accumulation results in CMC specimens using both micro-CT and acoustic damage.³⁵ For this work, AE was used in order to conserve the amount of time spent on each specimen as x-ray imaging can be time consuming.

Once the projection images were recorded from the beamline, the reconstruction of each image was performed using the reconstruction software package-Octopus (inCT, Universiteit Gent, Gentsesteenweg, 9300 Aalst, Belgium) at the ALS. The reconstruction process produced tomography images of the composite with a resolution of 1.3 $\mu\text{m}/\text{pixel}$ within a 3.28 mm x 2.8 mm field of view. A full 3D volume set of the specimen is created by stacking together 1025 projection images, or slices and the final datasets were analyzed using Avizo software.

RESULTS

Initial Observations

Two unidirectional (UD) specimens were imaged at increasing stress increments while under tensile load at the ALS. The stress increments at which the two specimens (arbitrarily labeled Sample A and Sample B) were imaged, are listed in Table I. Both Sample A and Sample B failed under tension within the scanned field of view and their corresponding stress-displacement curves are shown in Figure 2. It can be seen in Figure 2 that Sample B was weaker than Sample A failing at approximately 480 MPa while Sample A had a failure stress of 610 MPa. Due to the framework of the tensile load frame, an extensometer was not used and therefore the stress for each specimen is plotted in the form of stress versus crosshead displacement. The apparatus used for these experiments was displacement controlled and Figures 3a and 3b show the load and displacement vs. time for Sample A and Sample B respectively.

Figure 4 depicts a general 3-D image of a UD specimen that is obtained using synchrotron radiation for imaging. In this 3D image, it can be seen that fibers run in a vertical direction and form the two 0° plies in the unidirectional. Fibers that were damaged during polishing can also be seen extended near the edge of the volume of the specimen. In order to analyze damage within the specimen, single 2D images (slices) are viewed from within the

entire volume of the 3D image stack. Examples of tomography slices from Sample A are shown in three different perpendicular planes referred to as coronal, sagittal, and transverse as labeled in Figure 5. The coronal plane is viewed from the front face of the specimen, with the fibers running in a vertical direction and each slice in the coronal plane is a location within a ply of the specimen. The slices within the sagittal plane are from the edge or thickness of the specimen where both plies along with the center matrix rich region can be seen. The transverse plane is perpendicular to the loading direction and the circles shown in the example slice in Figure 5 depict the fibers.

Figure 6 shows the progression and accumulation of matrix cracks viewed in the coronal plane that occurred in Sample A at four increasing stress increments. Figure 6a is a slice from a scan taken before any damage occurred within the specimen at a stress of 10 MPa. The first matrix crack, represented by the blue arrow in Figure 6b, appeared in tomography scans at a stress of 400 MPa. By 475 MPa there were three new matrix cracks, depicted by three black arrows in Figure 6c, that developed above the initial matrix crack which can still be seen near the bottom of the slice. At 550 MPa, shown in Figure 6d, which shows a total of nine through matrix cracks that occurred across the entire thickness of the specimen. This was the last stress increment that was scanned for Sample A before it failed at 610 MPa. The crack with the red arrow in Figure 6d is the matrix crack that later caused failure at 610 MPa. The total number of matrix cracks measured at each stress increment is shown in Figure 7 in terms of the specimen's % of failure stress. Due to Sample B being weaker than Sample A, the results are plotted as a function of the percent of each sample's failure stress in order to directly compare the damage accumulation between the two specimens. At 80-85% of each specimen's failure stress, they both had five through thickness matrix cracks measured in the field of view. However, Sample B only had one more crack appear at a higher stress increment before the specimen failed but Sample A ended up having nine total matrix cracks in the field of view at 550 MPa, which was the last stress increment scanned before the specimen failed.

Fiber Breaks

Individual fiber breaks were observed within the volume of each specimen. Examples of fiber breaks from within Sample A are shown in Figure 8. There is a small gap between the ends of the broken fibers and these gaps show up in distinct dark contrast, with a bright white border due to micro-CT artifacts. Fiber breaks were segmented using Avizo software and black/gray contrast. Using the segmentation tool in Avizo, the software determines the x, y, z position of the centroid of each individual break in the volume of each composite specimen. Here the fibers run vertically along the z-direction, y is the direction of the 3mm wide specimen face, and x is direction of the 0.4 mm specimen thickness. Figure 9a represents the location of approximately 300 fiber breaks that were measured in scanned field of view from Sample A at the stress load of 445 MPa on a 3D plot. Figure 9b represents that same 3D scanned field of view for Sample A but at a stress of 550 MPa where there were over 2,000 fiber breaks measured.

The total number of fiber breaks within the 2.8 mm x 3.3 mm field of view was determined for both samples at each scanned stress increment. Figure 10 shows the number of breaks observed within the field of view for both specimens as a function of the % of failure stress. When comparing the number of fiber breaks in each specimen that occurred at increasing stress increments, it can be seen that there is good agreement. Between 75-80% of both specimens failure stress, there were approximately 400 measured fiber breaks. The number of fiber breaks increased drastically for both Sample A and Sample B between 85% and 100% of each of their failure stress. There were approximately 3,000 fiber breaks measured in both specimens post fracture, or 100% of their failure stress. For both Sample A and Sample B, there appears to be a linear trend in the number of fiber breaks as the applied stress, or % of failure stress, increases.

The 2-dimensional locations of all the fiber breaks and matrix cracks, relative to a common reference zero, measured in Sample A at 445 and 550 MPa are shown in Figures 11a and 11b respectively. The black lines represent the average location of the measured matrix cracks while the open black circles represent the 2D locations of fiber breaks in the coronal plane. Note, though many breaks in the top of Figure 11b are greater than 500 um from the nearest crack, one must recall that the field of view for imaging is 2.8 mm x 3.3mm while the

actual gauge section of the specimen is 3.0 mm x 9.0 mm. Therefore, some of the fiber breaks that are located in the upper portion of Figure 11b, at a location of 2000-3000 μm in the Y direction, may correlate to matrix cracks that are not visible in the scanned field of view but rather to a matrix crack outside of the field of view.

Knowing the location of all of the matrix cracks and fiber breaks within the composite, allows for a specific fiber break to be sorted in relation to the nearest matrix crack. Fiber breaks were sorted and binned based on proximity to matrix cracks. Using the positions of the fiber breaks and the matrix cracks, the distance of each fiber break from its related matrix crack was determined and the number of fiber breaks that occur within a range (i.e. 0-100 μm) away from a matrix crack are plotted in Figure 12. This was done for all nine of the matrix cracks that were observed at 550 MPa, directly before fracture. From this plot, it can be seen that at 550 MPa, most of the fiber breaks that were measured are located within a 100 μm distance of the nearest matrix crack.

DISCUSSION

It is well-documented in the literature, that for unidirectional composite specimens loaded in the fiber direction, the mechanical properties typically follow the rule of mixtures shown in Equation 1 where σ is the applied composite stress, v_f and v_m are the volume fractions of the fiber and matrix respectively while E_f and E_m are the young's modulus for each constituent. Values for modulus of SiC fibers and matrices found in the literature are in the range of 380-420 GPa and \sim 340-380 GPa respectively³²⁻³⁴. Prior to any damage occurring within the specimen, the far-field strain in the matrix and fiber are equivalent and the stress in the matrix and fibers can be determined from Equation 2 where σ_f and σ_m are the stress in the fiber and matrix. Using a Young's modulus of \sim 380 GPa and \sim 400 GPa for the matrix and fibers respectively results in a composite modulus of 395 GPa. At a lower applied stress of 200 MPa, before any major damage occurs and the sample can be assumed to have elastic behavior and Equation 2 can be used to approximate the matrix stress as 185 MPa and the fiber stress at 210 MPa. The stress in both the fiber and the matrix, before matrix cracking occurs, is of similar value because both constituents have similar elastic moduli values.

$$\sigma = v_f \sigma_f + v_m \sigma_m \#(1a)$$

$$E_c = v_f E_f + v_m E_m \#(1b)$$

$$\frac{\sigma}{E_c} = \frac{\sigma_f}{E_f} = \frac{\sigma_m}{E_m} \#(2)$$

The first matrix crack appeared in the image set taken at 400 MPa for Sample A and 375 MPa for Sample B. Matrix cracking occurs with simultaneous debonding between the fiber and matrix interface and theories suggest that debond length depends on the interfacial shear stress τ_s , interface toughness, and the stress on the fiber.^{10,36,37} However, since x-ray tomography is based on x-ray attenuation and the attenuation of the BN coating is so low that it appears black, there is no way to discern between the fiber coating and the debonding and therefore the fiber/matrix debonding is not detectible using these micro-CT techniques.

Utilizing micro-CT has shown that matrix cracks that occur through the volume of each specimen as applied stress is increased are quite tortuous, can bifurcate, and matrix cracks spaced close together can merge within the specimen. Most 2D images of matrix cracks from a polished surface using standard microscopy techniques don't present an accurate representation of the tortuosity of the matrix crack plane. In Figures 6a-d it can be seen that while most of the matrix cracks occur through the entire width of the specimen, there are some that do not and some of the through thickness matrix cracks have bifurcation that occurs within the specimen. For this work a matrix crack was only considered if it fully fractured across the width and thickness of the entire sample. The red arrow in Figure 6d signifies the matrix crack that eventually led to fracture in Sample A. Looking at tomography slices lower stresses, for example a coronal slice at 490 MPa in Figure 6c, the future failure crack is similar to the other matrix cracks that have occurred although this observation is limited by the resolution of the tomography image. Detailed observations and comparisons of matrix crack formation and accumulation between the two samples are discussed in Henson et al.³⁸

As stated earlier the first matrix crack was seen at 400 MPa and 375 MPa for Sample A and B respectively and the number of matrix cracks increased in each sample with applied stress which also results in a decrease in matrix crack spacing. The stress in the matrix at the matrix crack plane is zero but as the applied stress is increased, the stress in the matrix will continue to increase away from the matrix crack plane until another matrix crack occurs. This

process will continue until matrix crack saturation is reached which is also considered the final matrix crack spacing of the composite. Previous studies often report values for matrix crack density and matrix crack spacing using the matrix cracks that are visible post-fracture. For these micro-CT observations, the matrix crack density ranged from 1.0-3.5 cracks/mm with the density increasing with increasing applied stress which corresponds well to other studies that have reported values in the range of 0.5-4.5 cracks/mm.³⁹ The crack spacing for each sample was 210 μm and 430 μm at the highest imaged stress before failure for Sample A and Sample B respectively. Chateau et al. used micro-CT to study damage accumulation in SiC/SiC mini composites and reported matrix crack spacing values of 250 μm .²⁶ The observations for these unidirectional composite specimens show comparable matrix crack densities.

Models have been developed to relate the spacing of matrix cracks to the debond length. The Budiansky, Evans and Hutchinson model of shear-lag in unidirectional CMCs was used to determine the debond length, ℓ , for each sample in this study. The debond length was calculated using Equation 3a and the debond stress, σ_d , determined from Equation 3b. The debond length was determined for Sample A and Sample B at applied stresses of 550 MPa and 430 MPa respectively which were the last imaged stress increments before failure for each specimen. For Sample A the debond lengths ℓ , was determined to be $\sim 200 \mu\text{m}$ while the debond length for Sample B was calculated as 120 μm respectively using a value of 15 MPa for τ_s and 4 J/m² was used for ζ_d , the debonding toughness. The observed matrix crack spacing for both samples at these same stresses (550 MPa and 430 MPa) were 210 μm and 430 μm . There seems to be a good agreement between the calculated debond length and the observed matrix crack spacing for Sample A at a composite stress of 550 MPa, directly before failure. However, Sample B, which was the weaker of the two specimens has a much larger matrix crack spacing when compared to the calculated debond length. It is most likely that the specimen failed before matrix crack saturation was obtained and therefore a direct comparison cannot be made.

$$\ell = \left(\frac{v_m E_m}{v_f E_c} \right) \frac{\sigma - \sigma_d}{2\tau_s} \quad \#(3a)$$

$$\sigma_d = 2v_f \sqrt{\frac{E_f E_c \zeta_d}{v_m E_m r}} \#(3b)$$

Matrix crack spacing can also be compared to the shear lag distance or the distance at which the matrix stress is equivalent to the stress that occurs in the undamaged region by rearranging equation 4a to solve for distance, z . For Sample A, using a constant matrix stress of 395 MPa, the shear lag distance was 254 μm which is slightly larger than the last measured matrix crack spacing of 210 microns. For Sample B, using a constant matrix stress value of 350 MPa the shear lag distance was calculated to be 225 μm compared to a final matrix crack spacing measured to be 430 μm . Once again, it is most likely that Sample B failed before matrix crack saturation was reached. Although the shear lag distance can be calculated and compared to the measured matrix crack spacing for each specimen, it is important to note that there will be a certain point where shear lag distances will overlap from neighboring cracks and the fiber/matrix will no longer return to the far-field strain state but instead the bulk strain of the composite will increase.

In most ceramic composite systems, the strain to failure of the matrix is lower than the fibers and therefore matrix cracking is the first damage mechanism to occur. Once matrix cracking occurs, the intact fibers bridge the matrix crack and carry all of the subsequent load which results in the fiber stress increasing as the composite stress increases. The average fiber and matrix stresses as a function of distance from the matrix crack, z , can be determined using Equations 4a and 4b where τ_s is the interfacial shear stress and r is the fiber radius.³⁶ Based on a fiber volume fraction of 28%, at an applied stress of 400 MPa, which was the lowest stress at which a matrix crack was imaged, the stress in the fibers at the location of the matrix crack ($z = 0$) was ~ 1430 MPa while the stress in the matrix would be zero.

$$\sigma_f(z) = \frac{\sigma}{v_f} - \frac{2\tau_s z}{r} \#(4a)$$

$$\sigma_m(z) = \left(\frac{2v_f}{v_m}\right) \frac{\tau_s z}{r} \#(4b)$$

After matrix cracking occurs, the intact fibers carry all of the load at the location of the matrix crack and with the stress on the fibers decreasing linearly with distance away from the matrix crack plane. Commercially available Hi-Nicalon Type S fibers have a fiber strength

between 2.6-3 GPa and a fiber failure strain of $\sim 0.7\%$.^{32-34,40} Composite failure is completely dependent on fiber failure and ceramic fiber strengths are highly stochastic. There have been studies done on the testing of these fibers and characteristic strengths of 2.5-4.5 have been reported.^{34,41} The increase in stress on the fibers results in fibers breaking near a matrix crack. The clear contrast of broken fibers compared to the x-ray density of the SiC fibers allows for accurate location detail of segmented fiber breaks. Conventional imaging of polished CMC sections often does not show in-situ fiber fractures and the fiber damage that it does capture could be due to polishing artifacts instead of the actual mechanics of the composite. Because of this, there is limited information related to both the number and location of failed fibers within a melt infiltrated SiC/SiC composite. It can be seen in Figure 8 that the gap, or fiber break height, can vary and a single fiber can be broken in more than one location.

The number of fiber breaks for each specimen increased rapidly as the applied stress was increased, shown in Figure 10. Based on an estimate of the volume fraction of fibers in this sample, there were ~ 3500 fibers in the field of view. At lower stresses of 445 and 475 MPa, $\sim 70-87\%$ of Sample A's failure stress, $\sim 87-91\%$ of the fibers were still intact. There were approximately 2300 fiber breaks at 90% of Sample A's failure stress shown in Figure 10, so only 33% of the fibers were still intact. At fracture for both specimens there were approximately 3000 fiber breaks measured which would assume almost all of the fiber had broken and the ones that didn't were no longer able to carry load. However, it is important to note that these percentages are based on the fiber breaks observed in the small scanned field of view and there are fiber breaks that occurred outside of the field of view that were not taken into consideration.

It has been shown that although quite a few fiber breaks occur, we have not yet noticed any particular microstructural feature that is correlated with fiber breaks. It was observed that fiber breaking occurs near matrix cracks. When looking at fiber breaks in relation to matrix cracks, it was observed that at a smaller stress of 475 MPa, most of the fiber breaks measured in Sample A occurred within 500 μm of a matrix crack. Previously, matrix crack spacing was compared to calculated debond length. We believe the debond length can also be compared to the location of fiber breaks in relation to each matrix crack. Using Equation 3 to calculate

debond length at a lower applied stress of 475 MPa results in a debond length of $\sim 150 \mu\text{m}$ which is much smaller than the $500 \mu\text{m}$ range that the fiber breaks fall into. Although the debond length doesn't compare well to the distance of fiber break locations from a matrix crack at this lower stress, it is possible that there are matrix cracks that occurred but are not visible in the dataset due to the limitations of the resolution. However, as the applied stress increases there are larger quantities of both fiber breaks and matrix cracks filling the entire field of view and most of the measured fiber breaks occur within 100 microns from the matrix crack which also falls within the calculated debond length of $200 \mu\text{m}$ calculated at the same applied stress. Additionally, these results are similar to published fiber pullout studies which showed fiber pullout values between $100\text{-}250 \mu\text{m}$.⁴⁰ Due to higher matrix crack density and the complexity of the many matrix cracks at high stresses it is difficult to accurately correlate each fiber break to a specific matrix crack. However, using the same technique the trends appear to be the same. A preliminary examination of the location of the fiber breaks within the volume suggest that fiber breaks are spatially random, and do not appear to be cluster but this work continues.

Utilizing micro-CT to image SiC/SiC composites allows for large amounts of detailed information to be examined in-situ. Matrix crack initiation was observed while the specimens were under tensile load. Fiber breaks were easily distinguishable and only occurred after the onset of matrix cracking. These breaks were quantified both in number and opening value. The matrix crack position and the total number of matrix cracks at each stress increment were measured. However, due to the resolution utilized in these scans, the matrix crack opening was not able to be measured accurately. In-situ tomography techniques will allow for a better understanding of damage accumulation in these materials in order to compare to life prediction models.

CONCLUSIONS

Microstructural features such as matrix cracking and fiber breaks were observed using in-situ computed x-ray tomography techniques. Matrix crack formation was examined at each stress increment and through failure. Both of the specimens failed in the field of view and the

matrix crack that caused failure was able to be identified. Average matrix crack measurements were made and compared to previous work done on SiC/SiC composite materials.

In-situ fiber breaks were observed and measured with the number of breaks increasing with applied stress showing nearly the same trend between both tested specimens. It was determined that although there were a large number of fiber breaks reported, compared to the total number of fibers in the field of view, the fraction of broken fibers was extremely small compared to the number of fibers still able to bridge a matrix crack. When compared to the location of a matrix crack, it was observed that most of the fiber breaks occurred with 100 μm distance of a matrix crack. Work is still being done to determine if fiber breaks occur randomly or if they are correlated.

REFERENCES

1. Corman GS, Luthra KL. Silicon melt infiltrated ceramic composites (HiPerComp™). In: Bansal NP, editor. Handbook of ceramic composites. Boston, MA: Springer, 2005; p. 99-115.
2. DiCarlo J.A, Yun H-M, Morscher G.N., Bhatt R.T., SiC/SiC composites for 1200°C and above. In: Bansal NP, editor. Handbook of ceramic composites. Boston, MA: Springer, 2005; p. 77-98.
3. Ohnabe H, Masaki S, Onozuka M, Miyahara K, Sasa T. Potential application of ceramic matrix composites to aero-engine components. Composites, Part A. 1999; 30(4):489-496.
4. Morscher GN, Pujar VV. Melt-infiltrated SiC composites for gas turbine engine applications. Proce. ASME Turbo Expo: Power Land, Sea, Air. 2004; 2:353-359.
5. Marshall DB, Cox BN, Evans AG. The mechanics of matrix cracking in brittle-matrix fiber composites. Acta Metall. 1985; 33(11):2013-2021.
6. Thouless MD, Evans AG. Effects of pull-out on the mechanical properties of ceramic-matrix composites. Acta Metall. 1988; 36(3):517-522.
7. Rajan VP, Zok FW. Matrix cracking of fiber-reinforced ceramic composites in shear. J Mech Phys Solids. 2014; 73:3-21.

8. Parthasarathy TA, Cox B, Sudre O, Pryzbyla C, Cinibulk MK. Modeling environmentally induced property degradation of SiC/BN/SiC ceramic matrix composites. *J Am Ceram Soc.* 2018; 101(3):973-997.
9. Meyer P, Waas AM. FEM predictions of damage in continuous fiber ceramic matrix composites under transverse tension using the crack band method. *Acta Mater.* 2016; 102:292-303.
10. Aveston J, Kelly A. Theory of multiple fracture of fibrous composites. *J Mater Sci.* 1973; 8:352-362.
11. Evans A, Zok F, The physics and mechanics of fiber-reinforced brittle-matrix composites. *J Mater Sci.* 1994; 29:3857-3896.
12. Longbiao L. Modeling first matrix cracking stress of fiber-reinforced ceramic-matrix composites considering fiber fracture. *Theor Appl Fract Mech.* 2017; 92:24-32.
13. Beyerle D, Spearing S, Zok F, Evans A, Damage and Failure in Unidirectional Ceramic-Matrix Composites. *J Am Ceram Soc.* 1992; 75(10):19-25.
14. Sorenson B, Evans R, Analysis of damage in a ceramic matrix composite. *Int J Dam Mech.* 1992; 2:246-271.
15. Meyer P, Waas AM. Measurement of in situ-full-field strain maps on ceramic matrix composites at elevated temperature using digital image correlation. *Exp Mech.* 2015; 55(5):795-802.
16. Zok F, Spearing S. Matrix crack spacing in brittle matrix composites. *Acta Metall Mater.* 1992; 40:2033-2043.
17. Sevener KM, Tracy JM, Chen Z, Kiser JD, Daly S. Crack opening behavior in ceramic matrix composites. *J Am Ceram Soc.* 2017; 100(10):4734-4747.
18. Morscher GN, Gordon NA. Acoustic emission and electrical resistance in SiC-based laminate ceramic composites tested under tensile loading. *J Eur Ceram Soc.* 2017; 37(13):3861-3872.
19. Morscher GN, Ojard G, Miller R, Gowayed Y, Santhosh U, Ahmad J, et al. Tensile creep and fatigue of Sylramic-iBN melt-infiltrated SiC matrix composites: retained properties,

- damage development, and failure mechanisms. *Compos Sci Technol*. 2008; 68(15-16):3305-3313.
20. Smith CE, Morscher GN, Xia Z. Electrical resistance as a nondestructive evaluation technique for SiC/SiC ceramic matrix composites under creep-rupture loading. *Int J Appl Ceram Technol*. 2011; 8(2):298-307.
 21. Mansour R, Maillet E, Morscher GN. Monitoring interlaminar crack growth in ceramic matrix composites using electrical resistance. *Scr Mater*. 2015; 98:9-12.
 22. Whitlow T, Jones E, Przybyla C. In-situ damage monitoring of a SiC/SiC ceramic matrix composite using acoustic emission and digital image correlation. *Compos Struct*. 2016; 158:245-251.
 23. Bale HA, Haboub A, Macdowell AA, Nasiatka JR, Parkinson DY, Cox BN, et al. Real-time quantitative imaging of failure events in materials under load at temperatures above 1,600°C. *Nat Mater*. 2013; 12(1):40-46.
 24. Larson NM, Zok FW. In-situ 3D visualization of composite microstructure during polymer-to-ceramic conversion. *Acta Mater*. 2018; 144:579-589.
 25. Bernachy-Barbe F, Gélébart L, Bornert M, Crépin J, Sauder C. Anisotropic damage behavior of SiC/SiC composite tubes: Multiaxial testing and damage characterization. *Composites, Part A*. 2015; 76:281-288.
 26. Chateau C, Gélébart L, Bornert M, Crépin J, Caldemaïson D, Sauder C. Modeling of damage in unidirectional ceramic matrix composites and multi-scale experimental validation on third generation SiC/SiC minicomposites. *J Mech Phys Solids*. 2014; 63(1):298-319.
 27. Aroush DRB, Maire E, Gauthier C, Youssef S, Cloetens P, Wagner HD. A study of fracture of unidirectional composites using in situ high-resolution synchrotron x-ray microtomography. *Compos Sci Tech*. 2016; 66(10):1348-1353.
 28. Mazars V, Caty O, Couégnat G, Bouterf A, Roux S, Denneulin S, et al. Damage investigation and modeling of 3D woven ceramic matrix composites from x-ray tomography in-situ tensile tests. *Acta Mater*. 2017; 140:130-139.

29. Larson NM, Zok FW. Insights from in-situ x-ray computed tomography during axial impregnation of unidirectional fiber beds. *Composites, Part A*. 2018; 107:124-134.
30. Carlton HD, Haboub A, Gallegos GF, Parkinson DY, MacDowell AA. Damage evolution and failure mechanisms in additively manufactured stainless steel. *Mater Sci Eng A*. 2016; 651:406-414.
31. Yun HM, DiCarlo JA. Comparison of the tensile, creep, and rupture strength properties of stoichiometric SiC fibers. *Ceram Eng Sci Proc*. 1999; 20(3):259-272.
32. Bunsell AR, Piant A. A review of the development of three generations of small diameter silicon carbide fibres. *J Mater Sci*. 2006; 41(3):823-839.
33. Dunn D. The effect of fiber volume fraction in HiperComp™ SiC-SiC Composites. Ph.D. Thesis, Alfred University. 2010.
34. Lamon J, Mazerat S, R'Mili M. Reinforcement of ceramic matrix composites: properties of SiC-based filaments and tows. In: Bansal NP, Lamon J. editors. *Ceramic matrix composites: materials, modeling, and technology*. Hoboken, NJ: John Wiley & Sons, Inc, 2014; p. 1-26.
35. Mailet E, Singhal A, Hilmas A, Gao Y, Zhou Y, Henson G, et al. Combining in-situ synchrotron X-ray microtomography and acoustic emission to characterize damage evolution in ceramic matrix composites. *J Eur Ceram Soc*. 2019; 39(13):3546-3556.
36. Budiansky B, Hutchinson JW, Evans AG. Matrix fracture in fiber-reinforced ceramics. *J Mech Phys Solids*. 1986; 34(2):167-189.
37. Budiansky B, Evans AG, Hutchinson JW. Fiber-matrix debonding effects on cracking in aligned fiber ceramic composites. *Int J Solids Struct*. 1995; 32(3-4):315-328.
38. Hilmas A, Henson G, Singhal A, Gao Y, Schuster M. In-situ observation of damage in unidirectional CMC laminates under tension. *Ceram Int*. (*In Review, Ceramics International*)
39. Morscher GN, Gordon NA. Acoustic emission and electrical resistance in SiC-based laminate ceramic composites tested under tensile loading. *J Eur Ceram Soc*. 2017; 37(13):3861-3872.

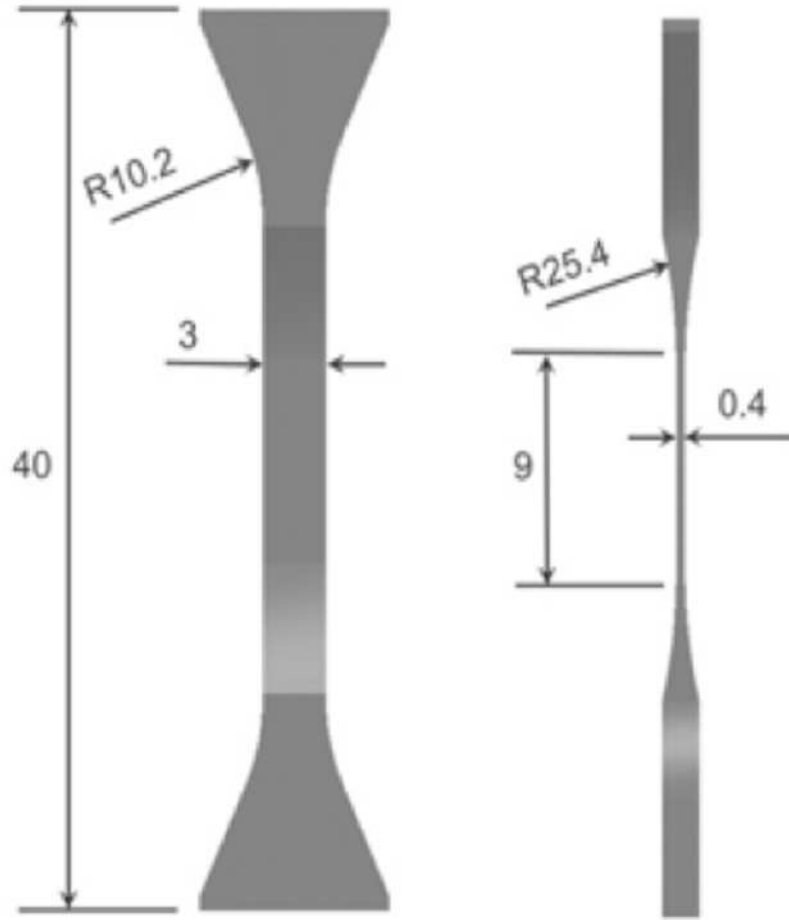
40. Meyer P. Experimental and numerical investigation of the damage response of ceramic matrix composites. Ph.D. Thesis, University of Michigan. 2015.
41. Hay RS, Chater RJ. Oxidation kinetics strength of Hi-Nicalon™-S SiC fiber after oxidation in dry and wet air. J Am Ceram Soc. 2017; 100(9):4110-4130.

FIGURE AND TABLE CAPTIONS LIST

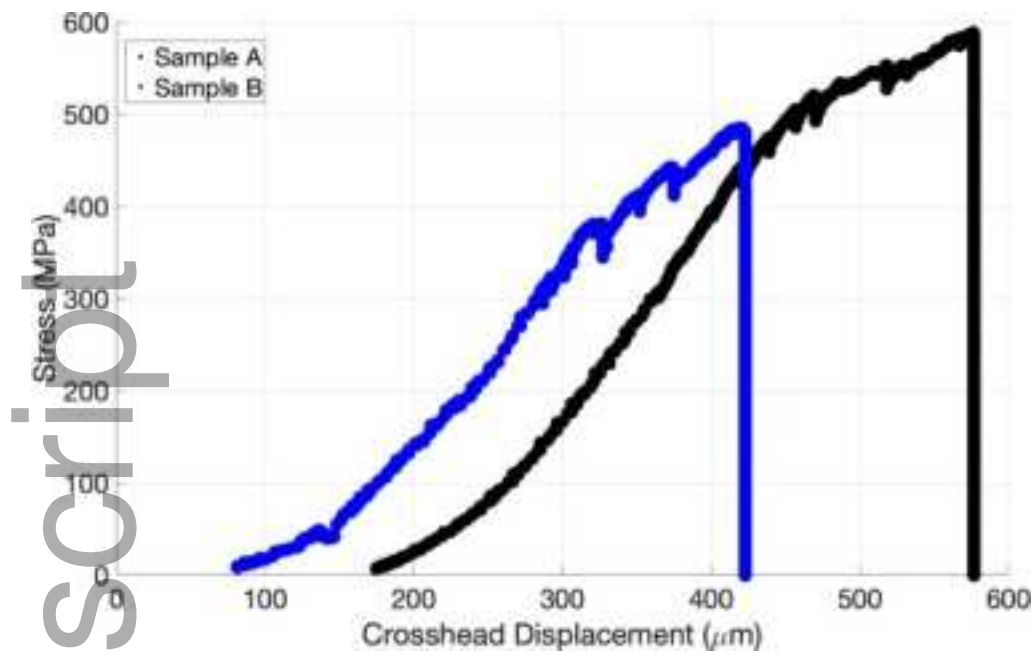
- Table I: Two unidirectional specimen were scanned and imaged at increasing stress increments
- Figure 1. Unidirectional composite specimen dimensions in mm
- Figure 2: Stress vs. Crosshead displacement for Sample A and B
- Figures 3a: Crosshead Displacement and Load vs. Time for Sample A
- Figures 3b: Crosshead Displacement and Load vs. Time for Sample B
- Figure 4: 3-D view of unidirectional specimen
- Figure 5: 2D images of Sample A to represent the three material directions. Each slice is taken ~ 200 microns into the thickness of the sample from each plane of view.
- Figure 6: crack progression shown from the coronal section in Sample A. This shows the full width of the specimen at slice 250 as stress on the specimen is increased. The blue arrows in Figure 6b and 6c show the initial through thickness matrix crack. The black arrows in 6c point to the three new matrix cracks that appeared at 490 MPa. The red arrow in Figure 6d represents the matrix crack that eventually led to fracture.
- Figure 7: total number of matrix cracks that occurred at increasing scanned stress increments shown as the % of each specimen's failure stress.
- Figure 8: Fiber Breaks in the unidirectional composite from sagittal view at 550 MPa (Slice 458 out of 2559).
- Figure 9a: 3D location of approximately 300 breaks measured at 445 MPa.
- Figure 9b: 3D location of approximately 2300 breaks measured at 550 MPa.
- Figure 10: total number of fiber breaks measured at increasing scanned stress increments shown as the % of each specimen's failure stress.

- Figure 11a: the position of fiber breaks (open circles) and matrix cracks (black lines) within the field of view of the specimen at 445 MPa.
- Figure 11b: the position of fiber breaks (open circles) and matrix cracks (black lines) within the field of view of the specimen at 550 MPa.
- Figure 12: The frequency of fiber breaks that occur within a distance from a particular matrix crack at 550 MPa.

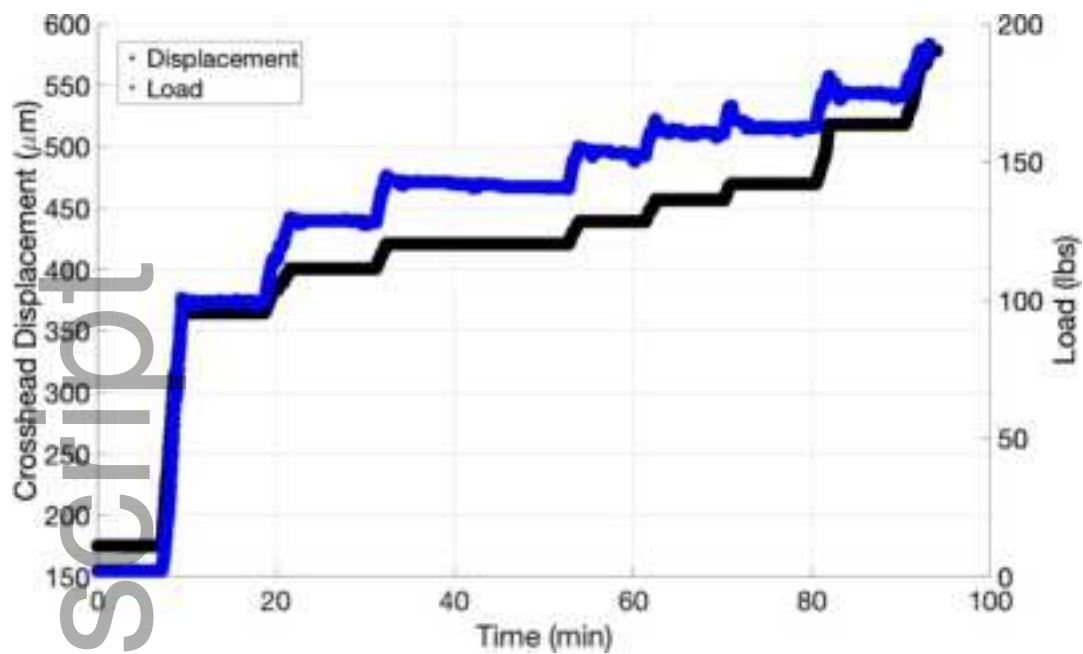
Author Manuscript



jace_17017_f1.tiff

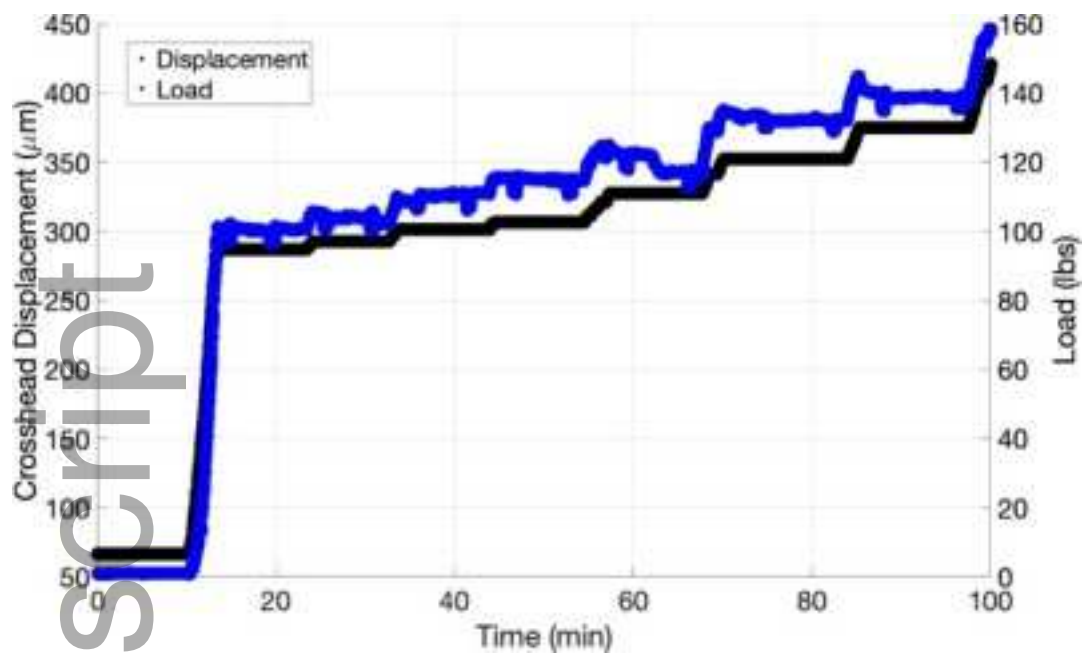


jace_17017_f2.tif



jace_17017_f3a.tif

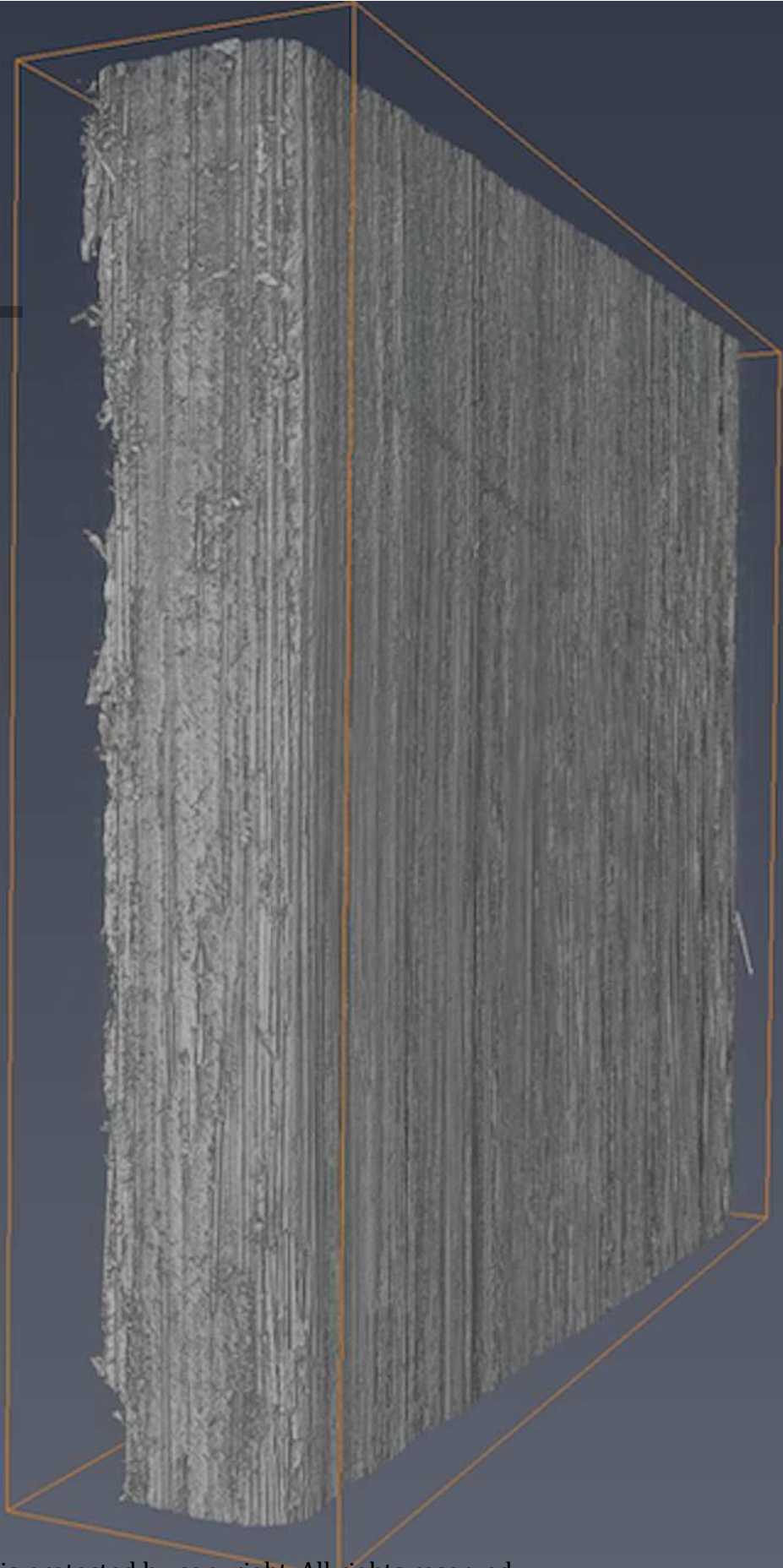
Author Manuscript



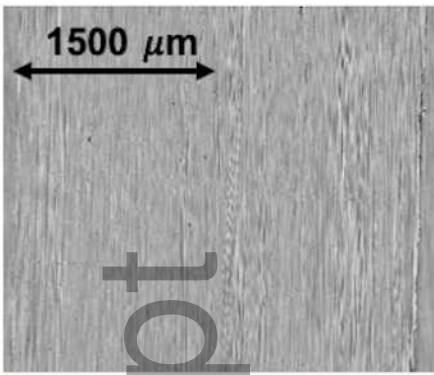
jace_17017_f3b.tif

Author Manuscript

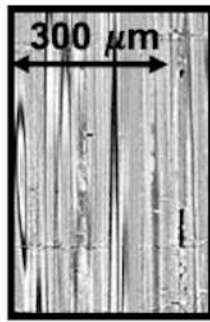
Author Manuscript



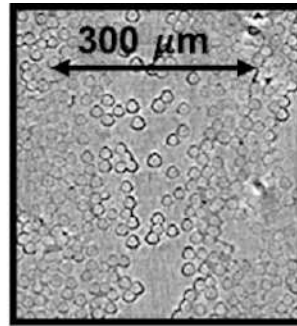
This article is protected by copyright. All rights reserved



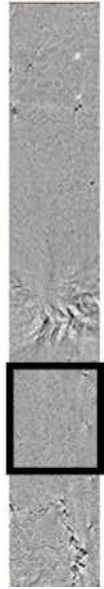
Coronal
Front face of Specimen



Sagittal
Side of Specimen

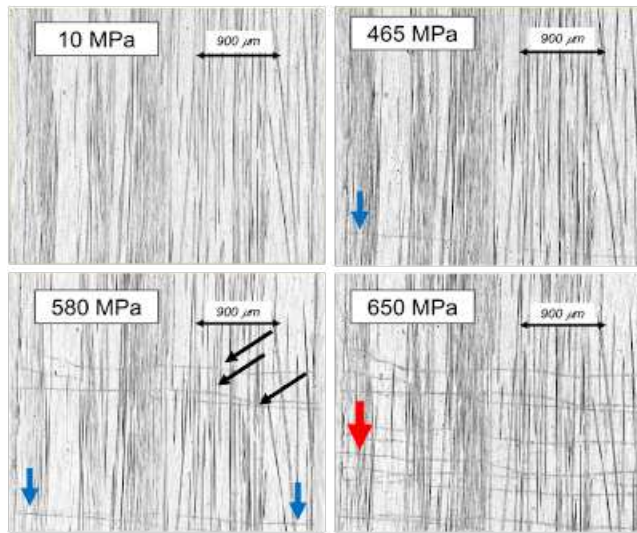


Transverse
Top of specimen

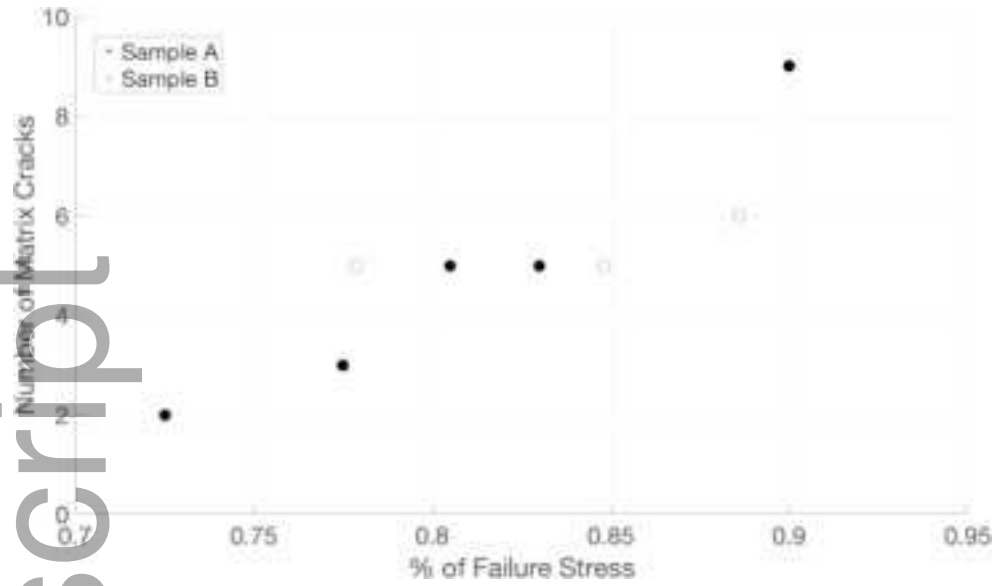


jace_17017_f5.tiff

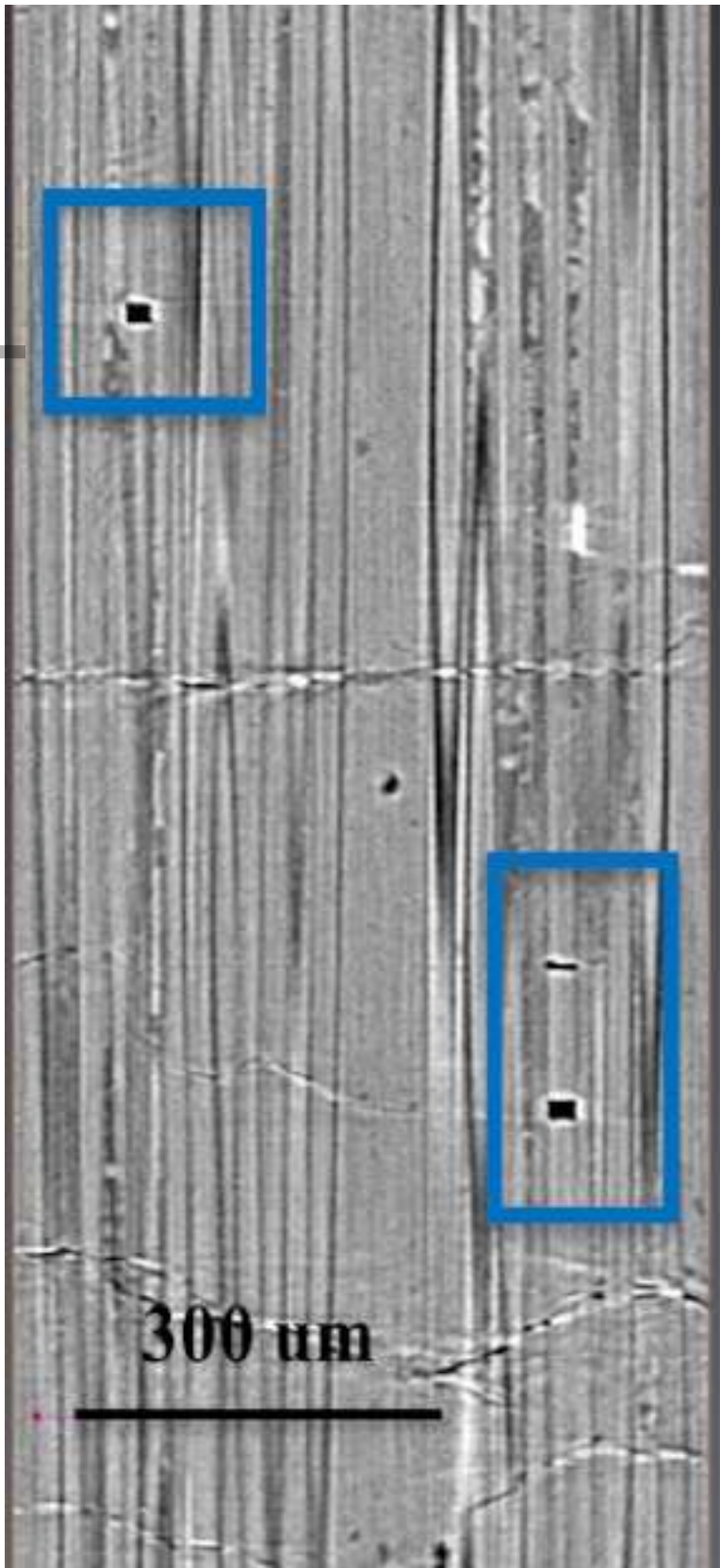
Author Manuscript



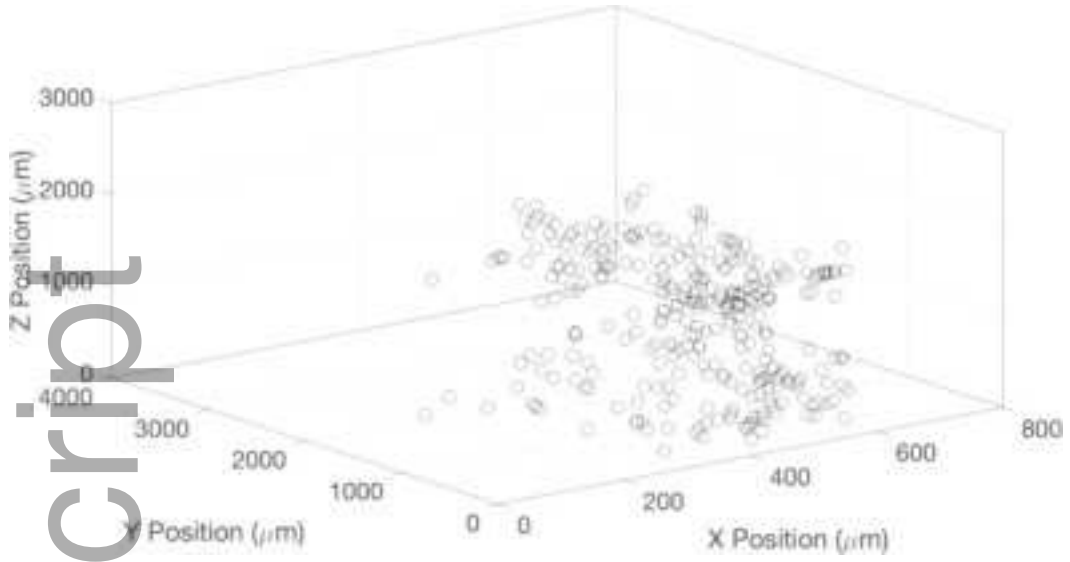
jace_17017_f6.tiff



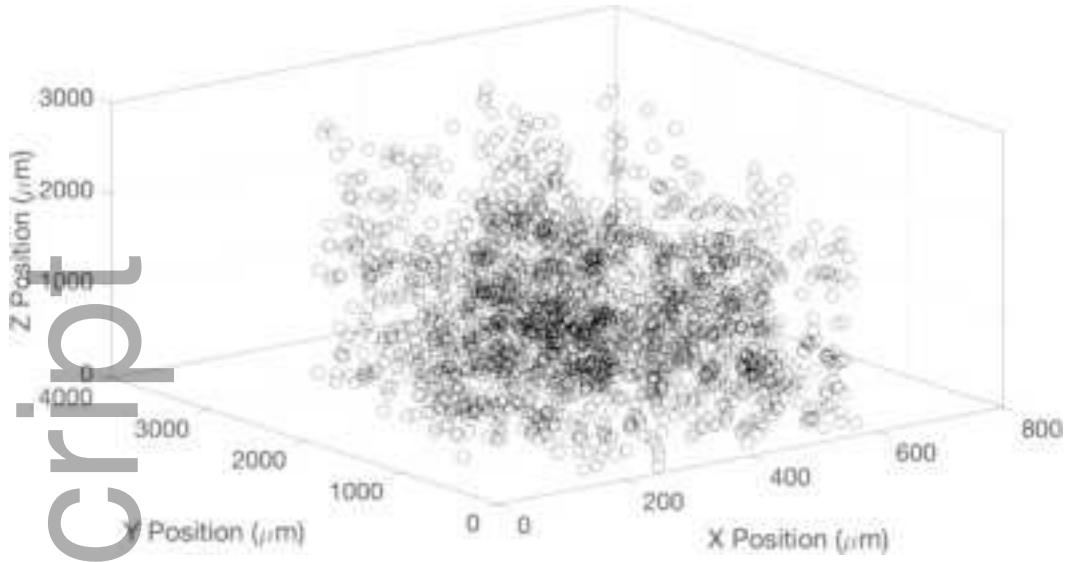
jace_17017_f7.tif



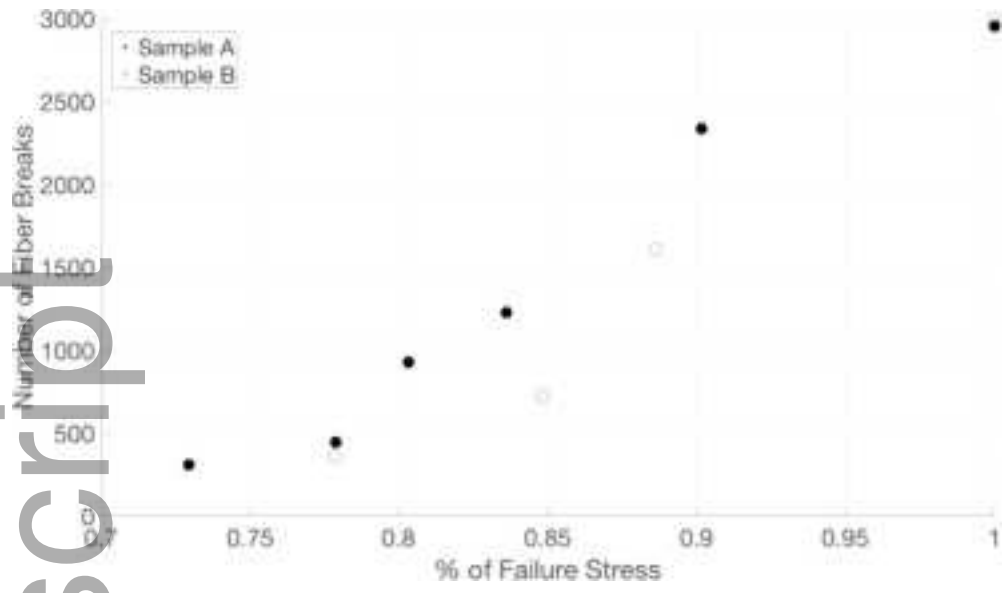
jace_17017_f8.tiff



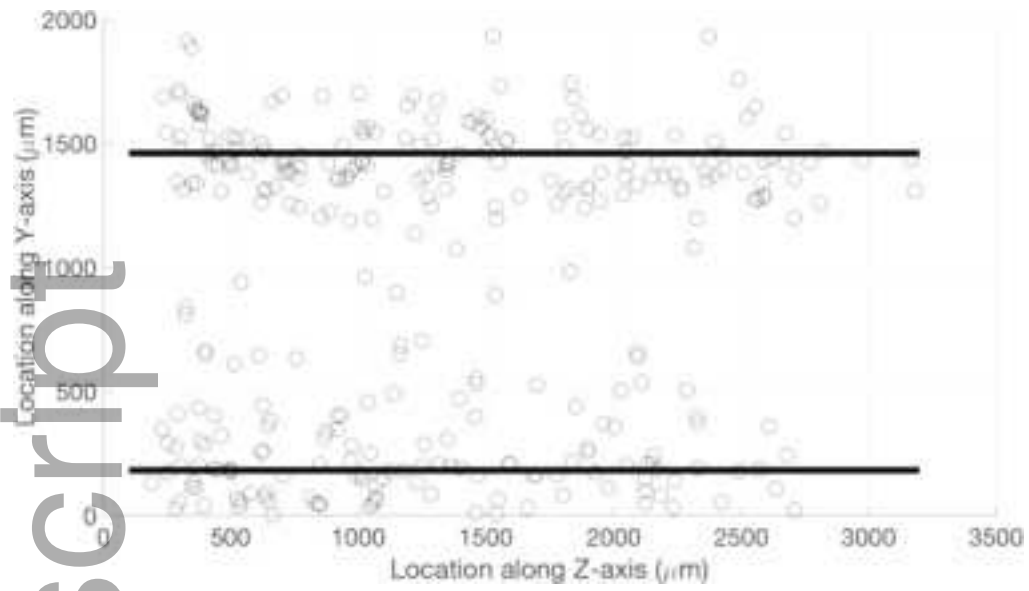
jace_17017_f9a.tif



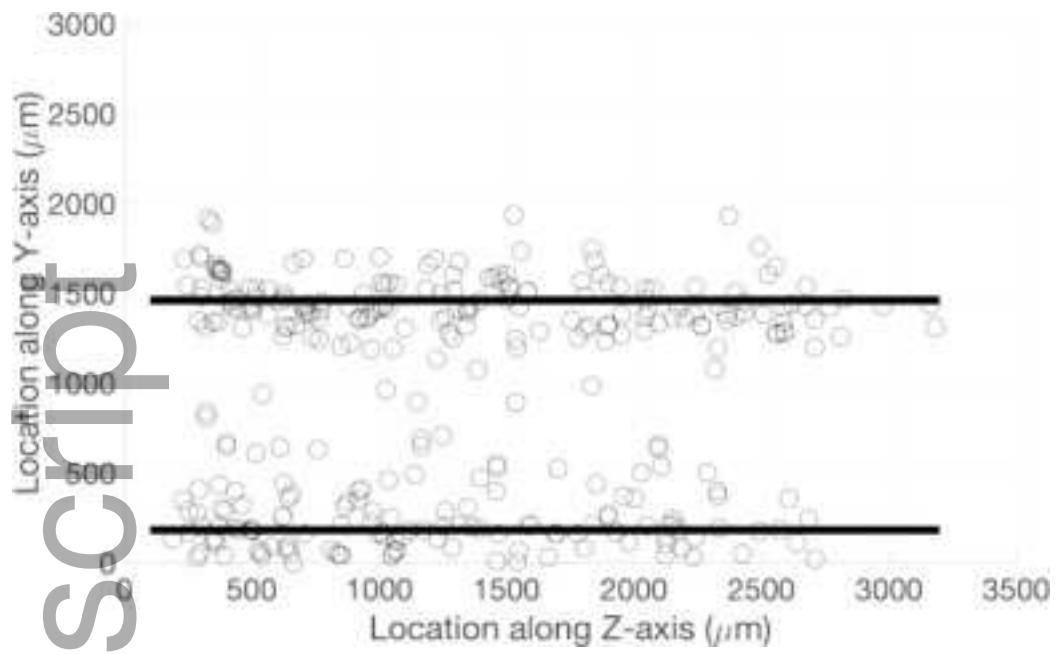
jace_17017_f9b.tif



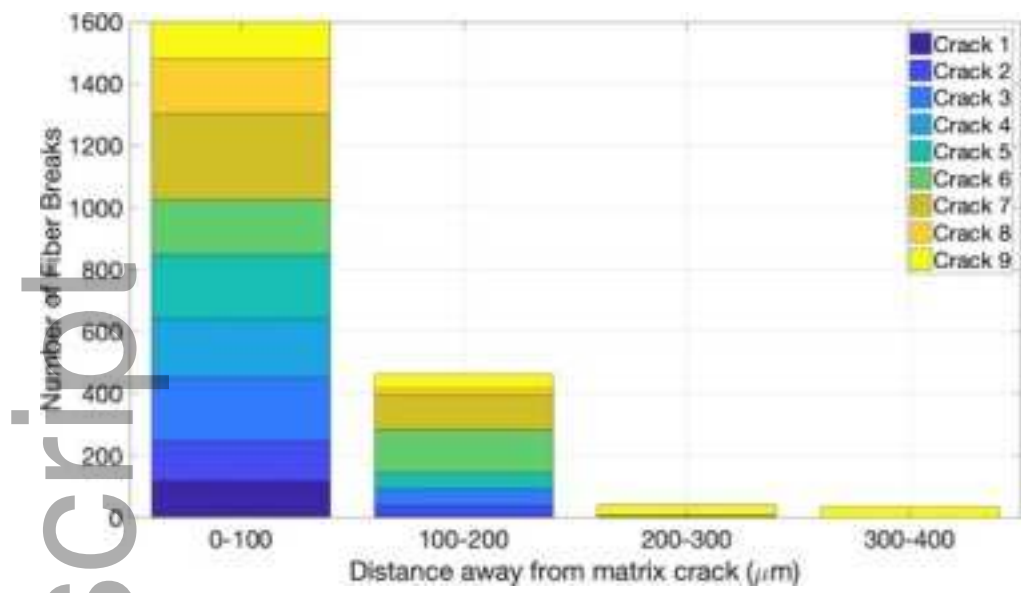
jace_17017_f10.tif



jace_17017_f11a.tif



jace_17017_f11b.tif



jace_17017_f12.tif